Selective laser melting of AlSi10Mg alloy: Process optimisation and mechanical properties development

Read, Noriko; Wang, Wei; Essa, Khamis; Attallah, Moataz M

DOI:
10.1016/j.matdes.2014.09.044

Selective Laser Melting of AlSi10Mg Alloy: Process Optimisation and Mechanical Properties Development

N. Read[1], W. Wang[1], K. Essa[2] and M. M. Attallah[1*]

[1]School of Metallurgy and Materials, University of Birmingham, Edgbaston, Birmingham, B15 2TT, UK.

[2]School of Mechanical Engineering, University of Birmingham, Edgbaston, Birmingham, B15 2TT, UK.

(*Corresponding author: Email: M.M.Attallah@Bham.ac.uk; Telephone: (+44) 121 414 7842)

Abstract

The influence of Selective Laser Melting (SLM) process parameters (laser power, scan speed, scan spacing, and island size using a Concept Laser M2 system) on the porosity development in AlSi10Mg alloy builds has been investigated, using statistical design of experimental approach, correlated with the energy density model. A two-factor interaction model showed that the laser power, scan speed, and the interaction between the scan speed and scan spacing have the major influence on the porosity development in the builds. By driving the statistical method to minimise the porosity fraction, optimum process parameters were obtained. The optimum build parameters were validated, and subsequently used to build rod-shaped samples to assess the room temperature and high temperature (creep) mechanical properties. The samples produced using SLM showed better strength and elongation properties, compared to die cast Al-alloys of similar composition. Creep results showed better rupture life than cast alloy, with a good agreement with the Larson-Miller literature data for this alloy composition.

Keywords: Selective laser melting; Aluminium alloys; Mechanical properties;

1. Introduction

Additive layer manufacturing (ALM) has been used for more than 30 years and is now widely used for various materials [1-4]. Although there are many types of production machines, they are all similar, in the sense that they produce three-dimensional shapes by combining a number of two-dimensional slices. In recent years, ALM has been developed for "rapid manufacturing" of metallic components using, electron beam melting (EBM), direct laser fabrication (DLF), and selective laser melting (SLM) [5, 6]. Aerospace manufacturers are focusing on the SLM powder-bed technology for Ti-alloy and Ni-superalloy components [7, 8] where the potential cost reduction, fewer steps in the production process and design-freedom are among the factors driving this technology. There has been an increasing number of reports on ALM of Al-alloys recently, because of the demand from the industrial field for lightweight structures with complex geometries [6, 9].

AlSi10Mg alloy is a traditional cast alloy that is often used for die-casting. Because of its high strength and good mechanical properties, this alloy has been widely used in the automotive and aerospace industry. Because of its near eutectic composition of Al and Si, it has good weldability. Mg plays an important role in age hardening as β′ and Mg_2Si (β-phase) [10]. Recently, various reports have been published of the microstructure using a processing parameter study of SLM-fabricated AlSi10Mg [11, 12].

There are many factors that affect the final quality of the SLM samples, including the feedstock material characteristics (powder size, morphology and size distribution). The laser heat input is another source important parameter, as it controls the degree of consolidation of the powder particles, or could potentially aggravate defect formation by creating turbulences in the melt pool that can form a keyhole-like defect in the extreme conditions. One of the approaches to represent the laser heat input is using the energy density function Ψ [6], which is given as

$$\Psi = \frac{P}{v \cdot h \cdot t} \tag{1}$$

where P and v are respectively the laser power and scan speed, h is scan spacing, and t is layer thickness. Some studies [3] used the energy density concept to correlate the porosity development with the heat input, but the trend was generally inconsistent, although it identified an optimum energy density level where the build density was the maximum.

Alternatively, the use of design of experiments (DOE) techniques such as the Response Surface Method, and statistical analysis using the analysis of variance (ANOVA), have been shown to be useful approaches to study the effect of many parameters in material processing applications. Response Surface design of experiment and ANOVA technique have been used for the significance of selective laser sintering (SLS) process variables on surface roughness [13]. Similarly, Carter [14] used response surface method and ANOVA techniques to optimise SLM for CMSX-486 Ni- superalloy, by studying the impact of the process parameters (laser power, scan speed, scan spacing and island size) on crack density and porosity fraction.

This paper focuses on the influence of SLM parameters for fabricating AlSi10Mg. Statistical experimental design was adopted to optimise the process parameters to minimise the defects (pores or cracks). Mechanical tests were performed on samples manufactured using optimised parameters that gave minimum porosity and voids. In this paper, the term "pore" includes spherical pores and irregular voids that are observed in the laser processed samples. The influence of the build orientation (vertically and horizontally built samples) on the tensile properties was investigated. In addition, high temperature mechanical (creep) properties were also measured for horizontally built samples.

2. Experimental Details

2.1 Material

The AlSi10Mg powder, the composition of which is shown in Table 1, was supplied by LPW Technology Ltd. The size range was 20 - 63 μm, as measured using Coulter LS230 laser diffraction particle size analyser.

Figure 1 (a) shows a Scanning Electron Microscope (SEM) micrograph of the powder. It is obvious that the powder particles are not spherical. The particles show a very irregular morphology, with many small irregular satellite particles attached to the big particles. These irregular shape with small satellite particles were observed elsewhere[15, 16]. The particle size distribution affects the powder flowability for in powder bed systems, as well as their melting behaviour [6]. Figure 1(b) shows the size distribution of the powder, which had an average particle size of ~35 μm. The slightly unsymmetrical distribution is potentially caused by the irregular powder morphology, and the potential agglomeration of the powder particles

during the measurement. Despite the irregular morphology, the powder had a reasonable flowability and Hausner's ratio for SLM.

2.2 Statistical Design of Experiment (DoE) using Response Surface

The response surface methodology is a statistical technique to generate an experimental design to find an approximate model between the input and output parameters, and to optimise the process responses (e.g. towards a maximum and a minimum). It is a collection of statistical and mathematical methods that are useful for modelling and analysing engineering problems. In this technique, the main objective is to optimise the response surface, which is influenced by various process parameters. The response surface Y can be expressed by a second order polynomial (regression) equation as shown in equation 2.

$$Y = b_o + \sum b_i x_i + \sum b_{ii} x_i^2 + \sum b_{ij} x_i \, x_j. \quad (2)$$

The experimental design procedure using the response surface methodology can be summarised as follows:

- Identification of the key process parameters.
- Selection of the upper and lower limit of the process parameters.
- Selection of the output response.
- Developing the experimental design matrix.
- Conducting the experiments as per the design matrix.
- Recording the output response.
- Developing a mathematical model to relate the process parameters with the output response.
- Optimising that model using genetic algorithm.

.

2.3 SLM

All specimens were fabricated using a Concept Laser M2 Cusing® SLM (laser powder-bed) system. The M2 system has a Yb-Fibre laser, with laser power up to 200 W, 150 μm laser track width, with laser scan speed up to 7000 mm/s. All specimens were built using a Z-increment (vertical) of 30 μm. All processing was carried out in an Argon atmosphere with an oxygen-content <0.1%. An "island scanning strategy" was adopted to fabricate specimens [17], in which the filled layer is divided into several square (islands) with each island being

built randomly and continuously. Inside each island, the laser is raster-scanned individually. After selective melting the islands, laser scans are carried out around the perimeter of the layer to improve the surface finish. For each subsequent layer, these islands are translated by 1 mm in the X and Y-directions, as illustrated in Figure 2. The aim of the island deposition strategy is to balance the residual stresses in the build [18].

2.4 Sample build and preparation

To perform the DoE and parametric optimisation, 27 parametric combinations were used to fabricate samples using a fractional factorial DoE. All samples were 10 mm × 10 mm × 10 mm cubes. Since Concept Laser M2 uses a dimensionless number hatch spacing a1 instead of scan spacing, a1 parameter was used for this study. a1 is defined as,

a1 (Hatch spacing) = Scan spacing *h*/ laser track width (constant, 150μm)

Table 2 shows the range and levels of the investigated key process variables.

2.5 Porosity and Microstructural Analysis

To characterise the area fraction and density of cracks and/or pores in the material, all samples were cut in the transverse direction (X-Y plane) 3 mm from the top of the build, mounted in conducting Bakelite, and polished to a 0.05 μm finish. Samples were analysed using a Zeiss Axioskop microscope, with an Axioskop 2® image analyser and AxioVision® software. For each sample, 25 images were collected from the centre. Image threshold was applied to determine the porosity content (porosity %), using ImageJ Software [19]. Table 3 summarises the findings of porosity % and the parametric combinations. No solidification cracks were observed, which was expected as AlSi10Mg alloy is has a generally low crack sensitivity [16], although oxide film crack-like features were observed. The microstructure of the samples was examined in a JEOL 6060 scanning electron microscope (SEM), equipped with a back-scattered electron (BSE) detector, and operated at 20 kV.

2.6 Mechanical testing

Rod-shape samples were fabricated using the optimised parameters that produced the lowest porosity. Samples were built vertically and horizontally, as shown in Figure 3. In the ‘vertical’ samples, the long boundary of the sample is parallel to the building direction, whereas the long boundary of the sample is perpendicular to the building direction in the ‘horizontal’ samples. Tensile tests were performed in accordance with BS EN 2002-1:2005 [20]. All

mechanical test results are the average of 3 samples. In addition, creep tests were performed at the following conditions 180˚C/200 MPa, 150˚C/200 MPa, and 180˚C/150 MPa for the horizontal samples, in according with BS EN 2002-5:2007 [21]. For each creep test, samples were kept at the test temperature for a minimum of 30 minutes prior to the test. For the 150˚C/200 MPa and 180˚C/150 MPa conditions, tests were stopped at 20 hours. Fracture surface observation was performed using SEM after the creep test.

3. Results and discussion

3.1 ANOVA results

The response surface for porosity is a function of laser power (P), scan speed (v), hatch spacing ($a1$), and island size (Z) and can be expressed as follows:

$$\text{Response} = b_o + b_1(P) + b_2(v) + b_3(h) + b_4(Z) + b_5(Pv) + b_6(Pa1) + b_7(PZ) + b_8(a1v) + b_9(vZ) + b_{10}(Za1) \quad (3)$$

where b_o is the average response, and b_1, b_2,.....,b_{10} are the model coefficients that depend on the main and interaction effects of the process parameters. The value of the coefficients for the porosity is shown in Table 4. The R^2-value, a measure of model fit, showed that each of the models described the relationship between the process parameters and porosity was 0.87. The ANOVA indicates that, within the investigated range of parameters, the porosity is mainly affected by laser power, scan speed and the interaction between the scan speed and hatch spacing. The island size was found unlikely to have any influence on porosity.

Figure 4 shows the response surface model prediction of porosity with respect to laser power and scan speed. It shows that decreasing the laser power and increasing the scan speed both result in an increased porosity. The influence of the laser power on porosity formation appears to be more significant at high scan speeds, and likewise the influence of the scan speed is more significant at lower laser power. A reduction in the laser power and an increase in the scan speed both have the effect of reducing the energy input into the material, as such these will result in the reduction of the melt pool which will lead to the formation of porosity due to the incomplete consolidation, and may ultimately lead to the breakdown of the SLM process. The relationship between energy input and porosity was also considered in Ti-alloys [22].

Figure 5 shows the interaction effect between the scan speed and hatch spacing on the porosity. A low hatch spacing a1 of 0.35 appears to eliminate the effect of the scan speed on the porosity; whereas a high hatch spacing a1 of 0.65 significantly increases the effect of scan speed on porosity fraction. Likewise, an increase in the hatch spacing will ultimately result in porosity formation due to the lack of sufficient overlap between the laser scan tracks, leading to incomplete consolidation. Since the laser power, scan speed, and hatch spacing can individually control the heat input, it is conceivable that porosity formation can be mitigated using one of these parameters (within the investigated process window) to increase the heat input (e.g. use slow scan speed to fully consolidate the melt pool). It is important to state that these deductions are only valid within the investigated process window, since other mechanisms for porosity formation (e.g. melt pool turbulence or evaporation) could be triggered outside the investigated range. By considering the results presented in Figure 4 and Figure 5, it can be seen that in order to eliminate or minimise the porosity within the material, a high laser power, at low scan speed with a small hatch spacing should be used.

3.2 Process Optimisation

During the optimisation, the objective function was set to minimise the porosity. The genetic algorithm was used to predict the process parameters based on the objective function. The equations modelling the response of porosity with respect to the four key process parameters (shown in equation 3 and the related coefficients listed in Table 4) were solved simultaneously. Figure 6 shows the contour plot for the optimisation function to obtain minimum porosity for a range of laser powers and scan speeds. Kempen *et al*. [11] suggested optimum process parameter of 200 W, 1400 mm/s, with scan spacing 105 μm. Additionally, Brandl *et al*. [23] used 250 W, 500 mm/s, 150 μm scan spacing, with 50 μm layer thickness to achieve defect-free SLM of the AlSi10Mg alloy.

3.3. Validation build

To confirm the relationship between the predicted optimum parameter sets and porosity, 5 samples were built using the optimised parameters. Table 5 shows the set of predicted parameters and the measured porosity. Figure 7 shows micrographs for samples D and E. In sample D, irregular shaped voids (some of them are 200-300 μm in size), rather than spherical, but the overall level of these irregular voids was very low. The irregular pores are most likely caused by improper powder spreading, especially as they were infrequent.

3.4 Mechanical tests

Figure 8 shows the tensile test results of horizontal and vertical samples together with data from die cast samples [24]. All samples were built using the parameters set E, shown in Table 5. There is no major influence for the build orientation on the tensile properties, although the horizontal samples show ~10% high strength. Figure 9 shows the time-strain curves of horizontal samples, for test conditions: (a) 180˚C/200 MPa, (b) 150˚C/200 MPa, and (c) 180˚C/150 MPa. All the strain–time relations show normal creep behaviour, such as primary, secondary and tertiary creep. For test condition (a), the sample ruptured at 18.7 h. Using creep rupture data [24] for Larson miller plot for the same alloy, the predicted rupture time was 14.8h.

Figure 10 shows the fractography of the samples tested to failure, for room temperature tensile tests (a,b) and creep tests (c,d). From these images, fracture surface are very rough and irregular. Deep cracks are generally obvious throughout the samples, interestingly all aligned in the same direction. At high magnifications, the fracture surface appears to contain a mix of small dimples and smooth areas. Moreover, fine unmelted powder particles are observed on both surfaces, Figure 10(b) and (d), which could be due to the presence of thick oxide layers on the particles, which did not enable a full consolidation to occur locally where they existed. These un-bonded regions give rise to large cracks in the failed samples. The fracture surfaces are very similar in both the tension and creep samples, although a larger number of deep cracks was observed in the samples tested in tension. Furthermore, the crack surfaces appear smoother in the tension samples, than those of the creep samples. Similar fracture surfaces have been observed in the SLM of AA6061 [16]. The influence of these un-bonded regions on the tensile properties is small, because their effect on the reduction of the load-bearing cross section is small, but these defects may influence fatigue properties, especially if they are formed near to the surface.

Figure 11 shows micrographs of the irregular voids. From the EDX data obtained from the areas arrowed in (b), it appears that area 2 is very high in oxygen, suggesting that this irregular void is associated with the presence of an oxide layer which prevented bonding. The

analysis for oxygen, particularly on a rough surface, will not be quantitatively accurate, but the large difference between area 2 and other areas is considered as highly significant.

3.5 Rationalising the Porosity Formation Using the Energy Density

Figure 12 shows a plot of porosity versus the energy density for the data previously provided in Table 2. The red dot indicates the predicted optimum parameter, E, previously provided in Table 5. The graph shows that at low energy density (<50 J/mm^3) corresponds to a high porosity due to the lack of consolidation. The porosity content then decreases with increasing the energy density. This result supports the energy threshold for the full consolidation shown by Figure 5. However, when the energy density exceeds approximately 60 J/mm^3, the porosity content starts to scatter beyond that level until 120 J/mm^3. In this region other defects, such as keyhole formation (due to vapourisation), have been observed within the material. Olakanmi also indicated that there is a certain threshold energy density that gives maximum material density, which is 60-75 J/mm^3 for Al, Al-Si and Al-Mg alloys [15]. Further in depth studies would be required to understand the factors governing this threshold level in various materials.

4. Conclusions

This study has shown the following:

- A statistical method has been used to evaluate the influence of process parameters on the porosity of SLMed AlSi10Mg, which shows the trends of porosity in the SLM fabricated samples.
- There is a critical energy density point that gives the minimum pore fraction for this alloy, approximately 60 J/m^3.
- The build direction does not strongly influence the tensile or creep strength of SLMed AlSi10Mg. Both building directions show higher strength than die cast A360, although the elongation is inferior to that of A360.
- Fracture surfaces show the presence of significant amounts of un-melted powder, which give rise to local cracking. Further work is required to see if it is possible to eliminate these regions.

Acknowledgements

The authors would like to acknowledge the financial support from MicroTurbo/Safran Group. The support of the Materials and Components for Missiles (MCM) Innovation and Technology Partnership (ITP, and the Defence Science and Technology Laboratory (Dstl) is highly appreciated.

References

[1] Casavola C, Campanelli SL, Pappalettere C. Preliminary investigation on distribution of residual stress generated by the selective laser melting process. The Journal of Strain Analysis for Engineering Design. 2009;44:93-104.

[2] Osakada K, Shiomi M. Flexible manufacturing of metallic products by selective laser melting of powder. International Journal of Machine Tools & Manufacture 2006;46:1188-93.

[3] Olakanmi EO, Cochrane RF, Dalgarno KW. Densification mechanism and microstructural evolution in selective laser sintering of Al-12Si powders. Journal of Materials Processing Technology. 2011;211:113-21.

[4] Yan C, Shi Y, Yang J, Liu J. Preparation and selective laser sintering of nylon-12 coated metal powders and post processing. Journal of Materials Processing Technology. 2009;209:5785-92.

[5] Vutova K, Vassileva V, Koleva E, Georgieva E, Mladenov G, Mollov D, et al. Investigation of electron beam melting and refining of titanium and tantalum scrap. Journal of Materials Processing Technology. 2010;210:1089-94.

[6] Liu A, Chua CK, Leong KF. Properties of Test Coupons Fabricated by Selective Laser Melting. Key Engineering Materials. 2010;447-448:780-4.

[7] Gu D, Wang Z, Shen Y, Li Q, Li Y. In-situ TiC particle reinforced Ti–Al matrix composites: Powder preparation by mechanical alloying and Selective Laser Melting behavior. Applied surface science. 2009;255:9230-40.

[8] Amato KN, Gaytan SM, Murr LE, Martinez E, Shindo PW, Hernandez J, et al. Microstructures and mechanical behavior of Inconel 718 fabricated by selective laser melting. Acta Materialia. 2012;60:2229-39.

[9] Dadbakhsh S, Hao L. Effect of Al alloys on selective laser melting behaviour and microstructure of in situ formed particle reinforced composites. Journal of Alloys and Compounds. 2012;541:328-34.

[10] Gupta AK, Lloyd DJ, Court SA. Precipitation hardening in Al – Mg – Si alloys with and without excess Si. Materials Science and Engineering 2001;A316:11-7.

[11] Thijs L, Kempen K, Kruth J-P, Humbeeck JV. Fine-structured aluminium products with controllable texture by selective laser melting of pre-alloyed AlSi10Mg powder. Acta Materialia 2013;61:1809–19.

[12] Kempen K, Thijs L, Humbeeck JV, Kruth J-P. Mechanical properties of AlSi10Mg produced by Selective Laser Melting Physics Procedia 2012;39:439 – 46

[13] Bacchewar PB, Singhal SK, Pandey PM. Statistical modelling and optimization of surface roughness in the selective laser sintering process. Proceedings of the Institution of Mechanical Engineers, Part B: Journal of Engineering Manufacture 2007;221:35-52.

[14] Carter LN. Selective Laser Melting of Ni-Superalloys for High Temperature Applications. Birmingham: University of Birmingham; 2013.

[15] Olakanmi EO. Selective laser sintering/melting (SLS/SLM) of pure Al, Al–Mg, and Al–Si powders: Effect of processing conditions and powder properties. Journal of Materials Processing Technology. 2013;213:1387-405.

[16] Louvis E, Fox P, Sutcliffe CJ. Selective laser melting of aluminium components. Journal of Materials Processing Technology 2011;211 275–84.

[17] Thijs L, Verhaeghe F, Craeghs T, Humbeeck JV, Kruth J-P. A study of the microstructural evolution during selective laser melting of Ti-6Al-4V. Acta Materialia 2010;58 3303–12.

[18] Hofmann Group. Hofmann Innovation Group Website - Concept Laser (http://www.hofmann-innovation.com/en/technologies/direct-cusing-manufacturing.html). 2012, accessed May 30th 2014.

[19] Rasband W. ImageJ. U. S. National Institutes of Health, Bethesda, Maryland, USA. http://imagej.nih.gov/ij, 1997-2014.

[20] British Standards Institution. Aerospace series. Metallic materials. Test methods. Tensile testing at room temperature (BS EN 2002-1:2005). 2006.

[21] British Standards Institution. Aerospace series. Metallic materials. Test methods. Tensile testing at elevated temperature (BS EN 2002-2:2005). 2006.

[22] Gong H, Rafi K, Starr T, Stucker B. The Effects of Processing Parameters on Defect Regularity in Ti-6Al-4V Parts Fabricated By Selective Laser Melting and Electron Beam Melting. The 24th

International SFF Symposium: An Additive Manfuacturing Conference. The University Of Texas at Austin 2013.
[23] Brandl E, Heckenberger U, Holzinger V, Buchbinder D. Additive manufactured AlSi10Mg samples using Selective Laser Melting (SLM): Microstructure, high cycle fatigue, and fracture behavior. Materials and Design. 2012;34:159-69.
[24] Kaufman JG. Properties of aluminum alloys : tensile, creep, and fatigue data at high and low temperatures. In: Kaufman JG, editor. Materials Park, Ohio ASM International ; Washington, D.C. : Aluminum Association 1999. p. 264.

List of Figure Captions

Figure 1 (a) SEM micrograph, showing the morphology of the AlSi10Mg powder, and (b) the powder size distribution.

Figure 2 Schematic illustration of the island scan strategy, showing (a) each layer is divided into square (islands) and the inside of island is raster scanned, then (b) the successive layers are displaced 1 mm in the X and Y-directions.

Figure 3 Schematic drawing of horizontal and vertical samples for the mechanical tests.

Figure 4 Response surface plot showing the effect of the laser power and scan speed on the porosity, at 0.5 hatch-spacing a1 and 5 mm island size.

Figure 5 The impact of the interaction effect of scan speed and hatch spacing on the porosity, at 150 W laser power and 5 mm island size. The solid lines represent model prediction while the dash lines represent the variation of the actual data around the model prediction.

Figure 6 Predicted optimum laser power and scan speed for minimum porosity.

Figure 7 Optical micrograph images of (a) sample D and (b) sample E shown in Table 5.

Figure 8 Tensile properties of SLM fabricated AlSi10Mg alloy, compared to die cast A360 alloy [24].

Figure 9 Creep curves of SLM fabricated AlSi10Mg alloy (horizontal samples) at the following conditions: (a) 180˚C/200 MPa, (b) 150˚C/200 MPa, and (c) 180˚C/150 MPa.

Figure 10 Backscattered SEM fractographs of SLM fabricated AlSi10Mg horizontal samples, showing (a) RT tensile test sample, (b) enlarged image, shown in yellow square in (a), (c) Creep test sample, tested at 180˚C/200 MPa and (d) enlarged image, shown in yellow square in (c). Dimples-containing areas are circled, and the smooth areas are labelled using white rectangles. Unmelted particles are arrowed.

Figure 11 Secondary electron SEM images of irregular shape porosity showing an oxide film defect. The areas numbered have been analysed using EDX, as shown in the table.

Figure 12 Porosity variation versus the energy density. The diamond points show the result of Table 3, and the circle shows the predicted parameter E, shown in Table 5.

List of Table Captions

Table 1 Chemical composition of the investigated AlSi10Mg alloy (Wt.%).

Table 2 The range of matrix building parameters.

Table 3 Response surface model coefficients for cracking density and porosity fraction.

Table 4 Matrix building parameters and %porosity.

Table 5 Predicted building parameter and actual porosity%.

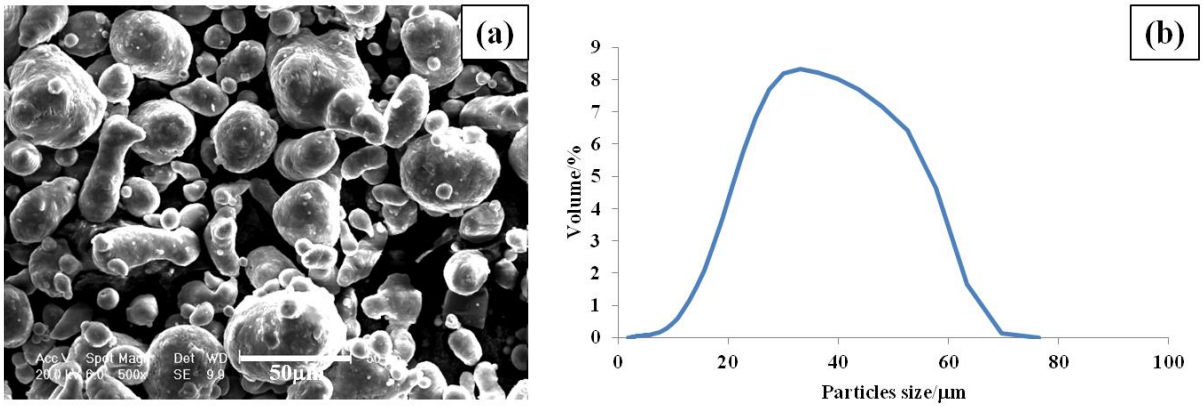

Figure 1 (a) SEM micrograph, showing the morphology of the AlSi10Mg powder, and (b) the powder size distribution.

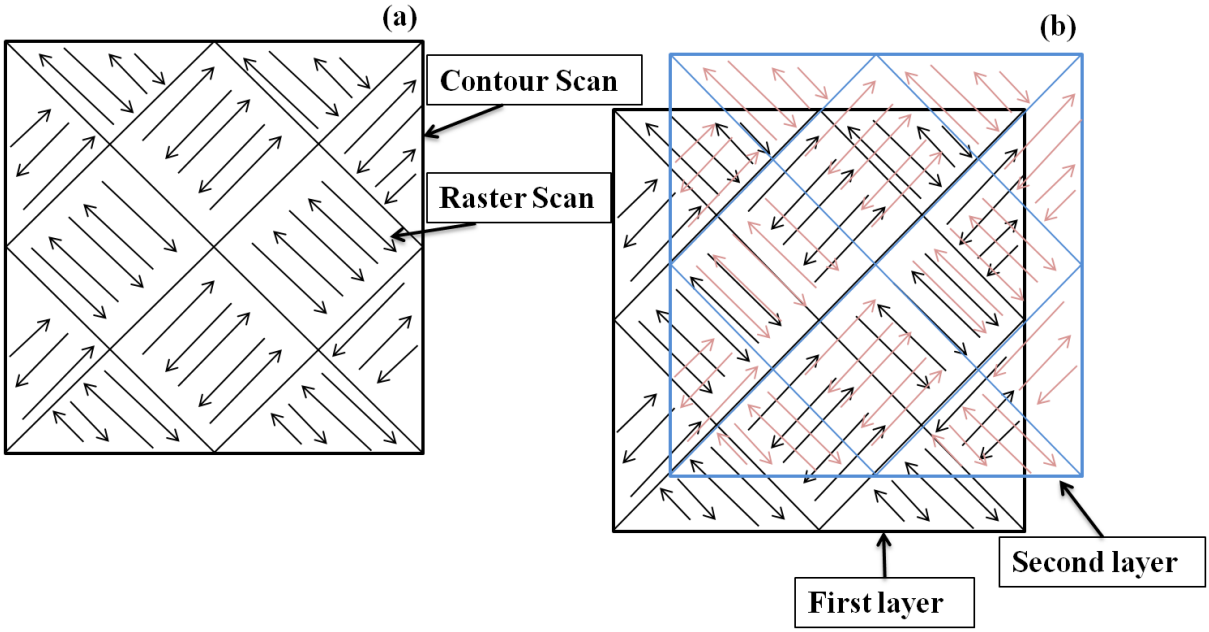

Figure 2 Schematic illustration of the island scan strategy, showing (a) each layer is divided into square (islands) and the inside of island is raster scanned, then (b) the successive layers are displaced 1 mm in the X and Y-directions.

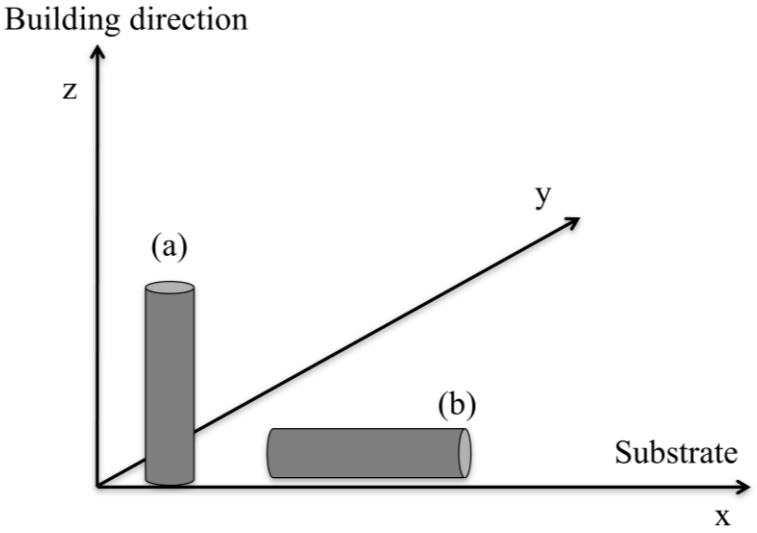

Figure 3 Schematic drawing of horizontal and vertical samples for the mechanical tests.

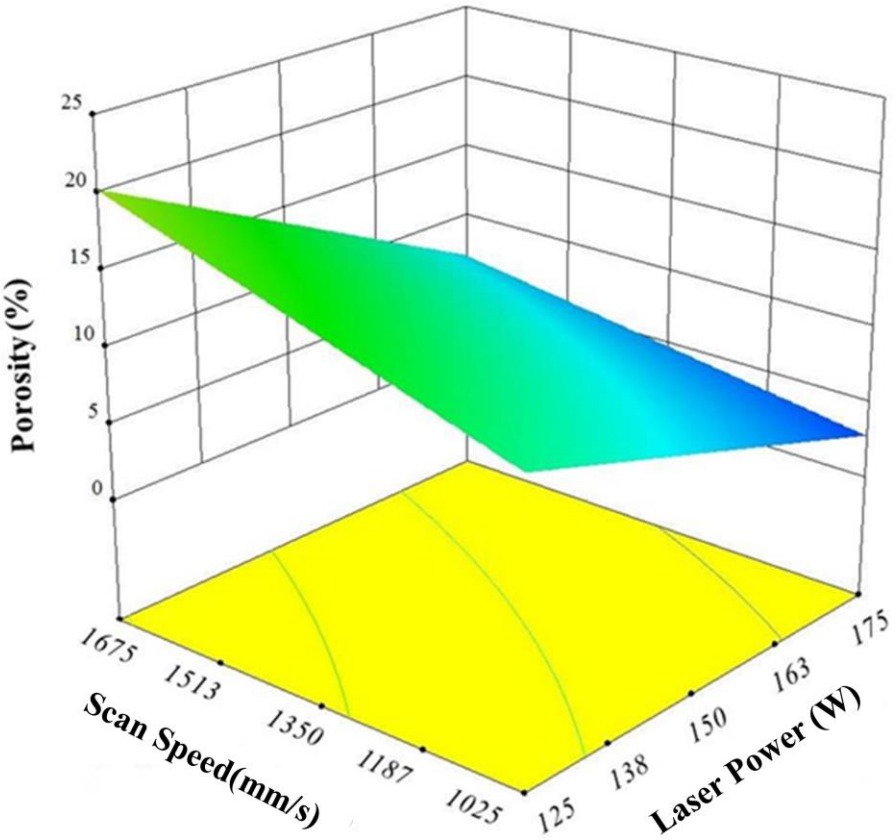

Figure 4 Response surface plot showing the effect of the laser power and scan speed on the porosity, at 0.5 hatch-spacing a1 and 5 mm island size.

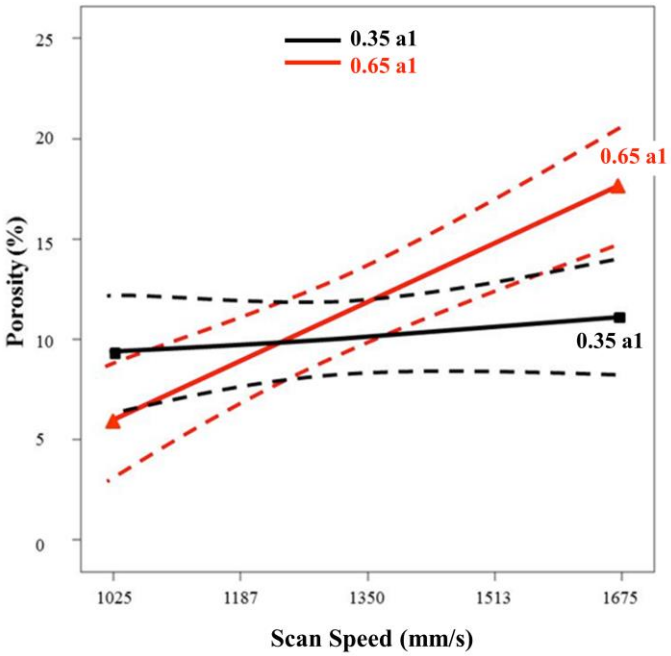

Figure 5 The impact of the interaction effect of scan speed and hatch spacing on the porosity, at 150 W laser power and 5 mm island size. The solid lines represent model prediction while the dash lines represent the variation of the actual data around the model prediction.

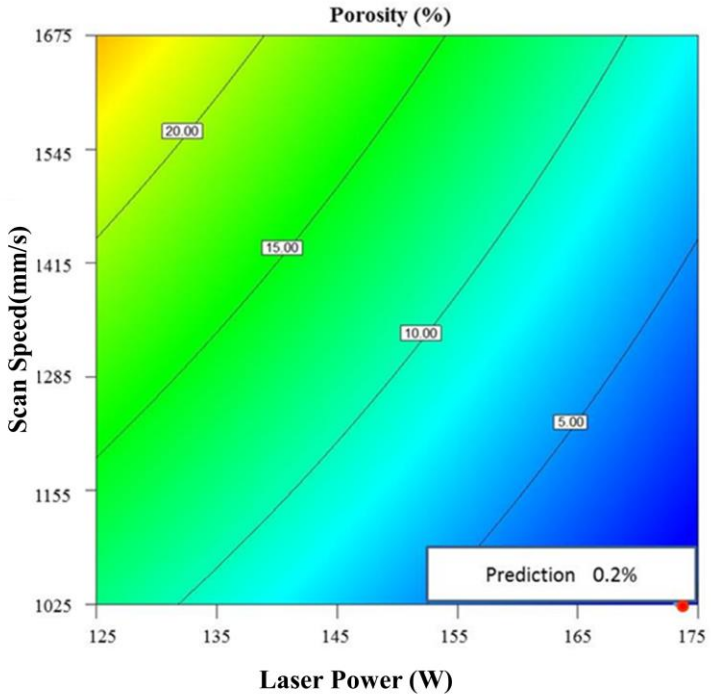

Figure 6 Predicted optimum laser power and scan speed for minimum porosity.

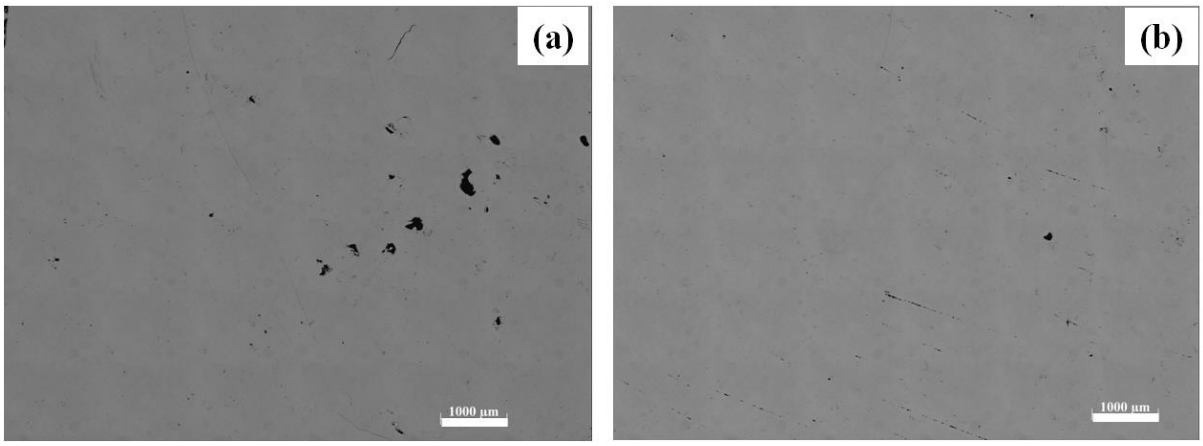

Figure 7 Optical micrograph images of (a) sample D and (b) sample E shown in Table 5.

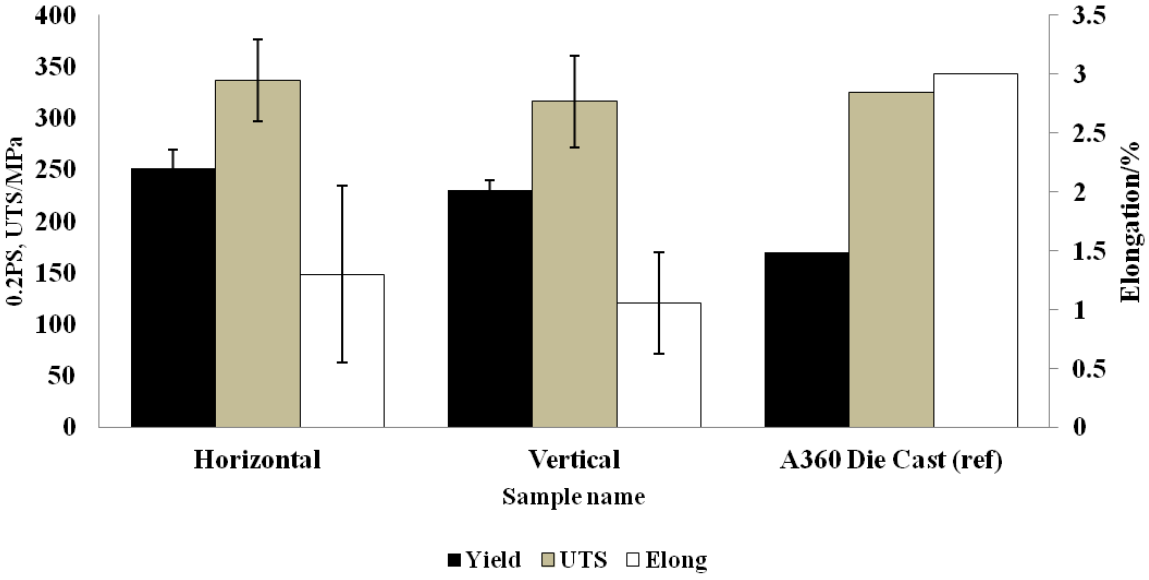

Figure 8 Tensile properties of SLM fabricated AlSi10Mg alloy, compared to die cast A360 alloy [24].

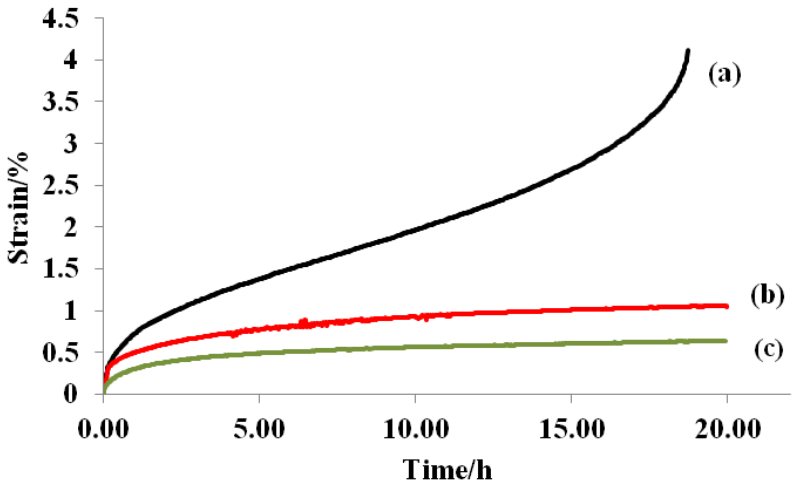

Figure 9 Creep curves of SLM fabricated AlSi10Mg alloy (horizontal samples) at the following conditions: (a) 180˚C/200 MPa, (b) 150˚C/200 MPa, and (c) 180˚C/150 MPa.

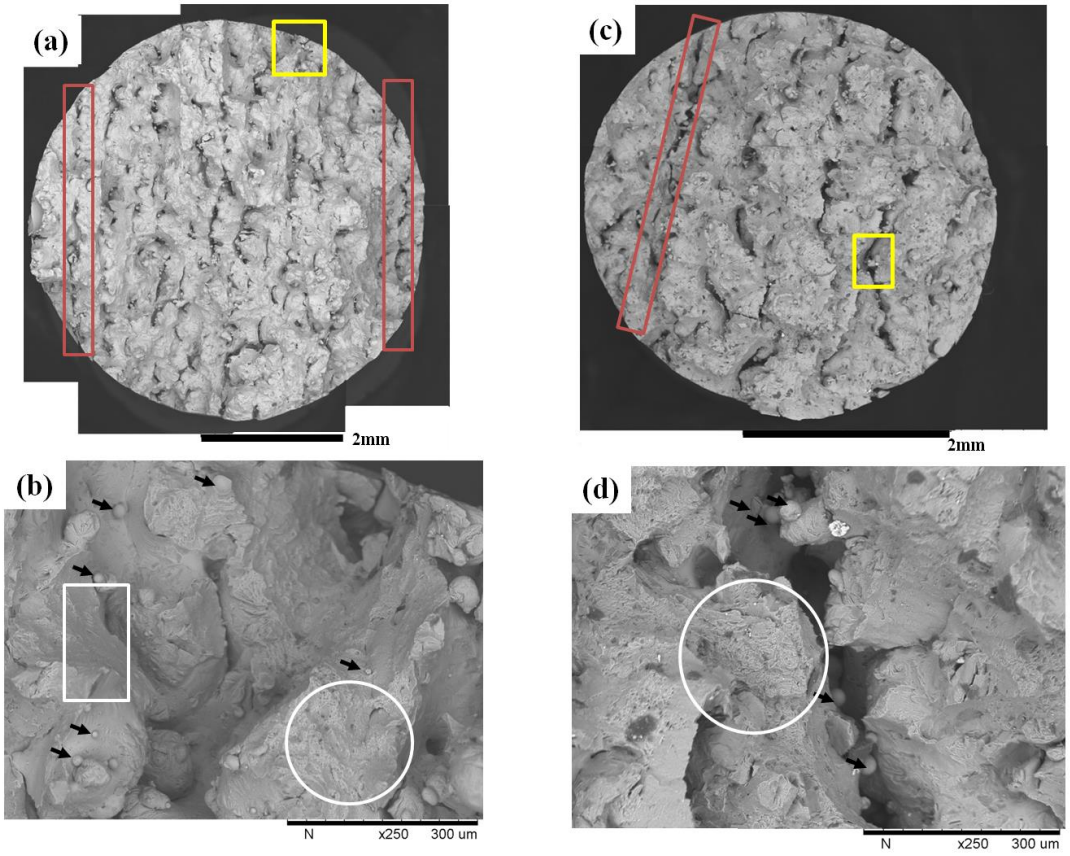

Figure 10 Backscattered SEM fractographs of SLM fabricated AlSi10Mg horizontal samples, showing (a) RT tensile test sample, (b) enlarged image, shown in yellow square in (a), (c) Creep test sample, tested at 180˚C/200 MPa and (d) enlarged image, shown in yellow square in (c). Dimples-containing areas are circled, and the smooth areas are labelled using white rectangles. Unmelted particles are arrowed.

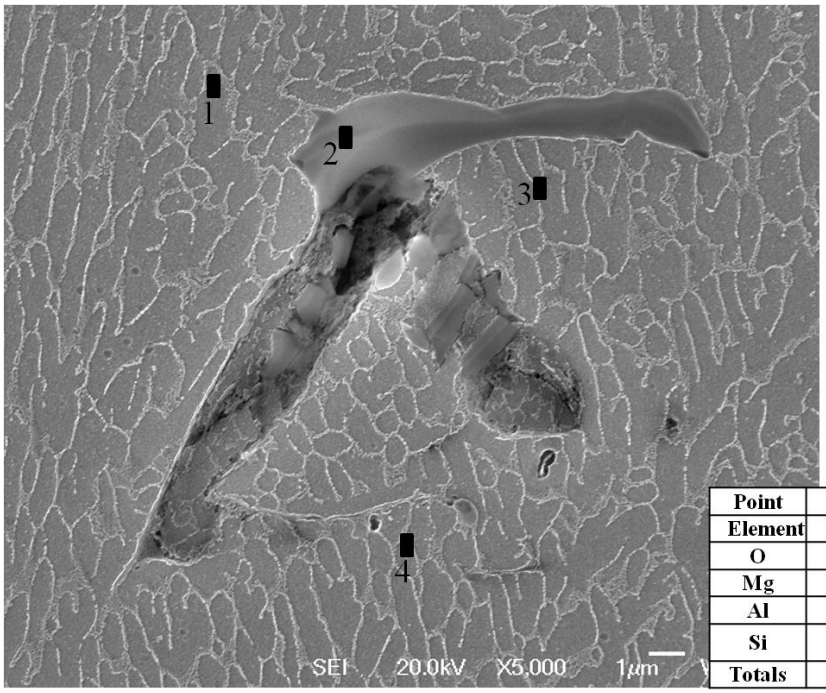

Point	1	2	3	4
Element	Wt.%	Wt.%	Wt.%	Wt.%
O	0.87	41.75	2.55	0.40
Mg	0.30	0.58	0.31	0.26
Al	88.57	56.42	86.96	88.17
Si	10.24	1.23	10.20	11.18
Totals	100	100	100	100

Figure 11 Secondary electron SEM images of irregular shape porosity showing an oxide film defect. The areas numbered have been analysed using EDX, as shown in the table.

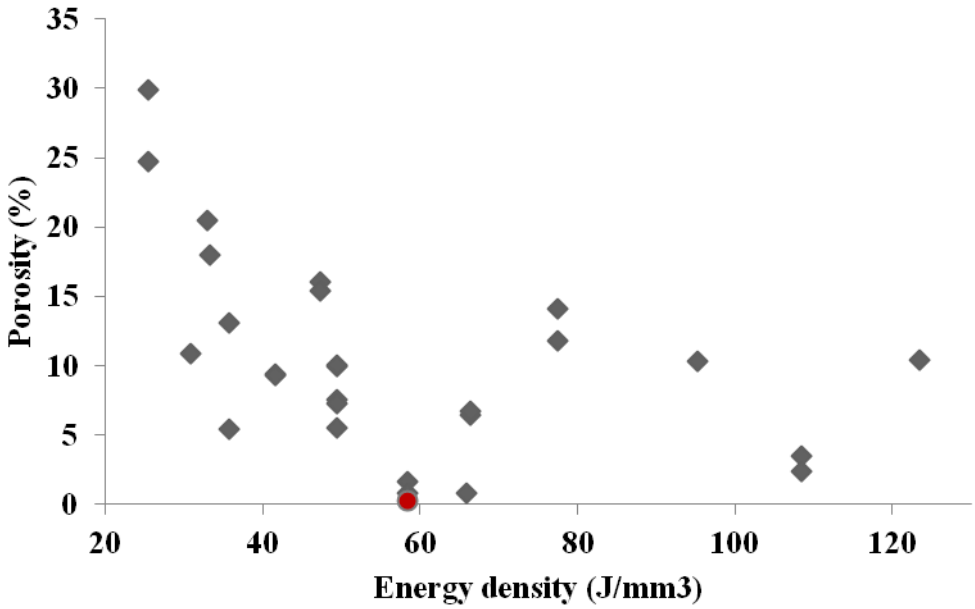

Figure 12 Porosity variation versus the energy density. The diamond points show the result of Table 3, and the circle shows the predicted parameter E, shown in Table 5.

Table 1 Chemical composition of the investigated AlSi10Mg alloy (Wt.%).

Si	Fe	Mn	Mg	Ni	Zn	Pb	Sn	Ti	Al
9.92	0.137	0.004	0.291	0.04	0.01	0.004	0.003	0.006	Bal

Table 2 The range of matrix building parameters.

Parameter	Units	Levels				
		-2	-1	0	1	2
Laser Power	W	100	125	150	175	200
Scan Speed	mm/s	700	1025	1350	1675	2000
Hatch Spacing	(a1)	0.2	0.35	0.5	0.65	0.8
Island Size	mm	2.0	3.5	5.0	6.5	8.0

Table 3 Response surface model coefficients for cracking density and porosity fraction.

Coefficient	**The Corresponding value**
b_o	-12.76
b_1	+ $2.07\times E^{-1}$
b_2	+ $1.02\times E^{-2}$
b_3	- 20.44
b_4	+ 5.50
b_5	- $1.39\times E^{-4}$
b_6	- $2.32\times E^{-1}$
b_7	- $2.4\times E^{-2}$
b_8	+ $5.01\times E^{-2}$
b_9	- $8.37\times E^{-4}$
b_{10}	- 1.45

Table 4 Matrix building parameters and %porosity.

Run	Laser power (W)	Scan speed (mm/s)	Hatch spacing a1 (h / 150 μm)	Island size (mm)	Porosity (%)
1	125	1675	0.35	6.5	16.1
2	125	1675	0.65	3.5	24.7
3	125	1025	0.65	6.5	9.4
4	150	1350	0.8	5	10.8
5	125	1675	0.65	6.5	29.9
6	150	700	0.5	5	10.4
7	150	1350	0.5	5	9.9
8	125	1675	0.35	3.5	15.4
9	175	1025	0.65	6.5	1.7
10	175	1675	0.65	6.5	5.5
11	125	1025	0.35	3.5	11.8
12	150	1350	0.2	5	10.5
13	125	1025	0.35	6.5	14.1
14	150	1350	0.5	2	7.5
15	100	1350	0.5	5	20.5
16	150	1350	0.5	5	10.1
17	175	1025	0.35	6.5	3.5
18	125	1025	0.65	3.5	9.3
19	175	1675	0.35	6.5	6.4
20	175	1675	0.65	3.5	13.1
21	200	1350	0.5	5	0.8
22	150	2000	0.5	5	18.0
23	175	1675	0.35	3.5	6.8
24	150	1350	0.5	5	5.5
25	150	1350	0.5	8	7.3
26	175	1025	0.65	3.5	0.8
27	175	1025	0.35	3.5	2.4

Table 1 Predicted building parameter and actual porosity%.

Sample	Power (W)	Scan Speed (mm/s)	Hatch spacing a1 (h / 150 μm)	Island size (mm)	Porosity (%)	
					Predicted	Measured
A	175	1035	0.65	5.9	0.2	0.37
B	173	1025	0.65	6.5	0.2	0.38
C	175	1030	0.64	6	0.2	0.46
D	174	1026	0.65	6.2	0	0.61
E	175	1025	0.65	5.6	0	0.29